Arabian Journal of Chemistry (2022) **15**, 104303

King Saud University

Arabian Journal of Chemistry

www.ksu.edu.sa
www.sciencedirect.com

ORIGINAL ARTICLE

An insight to the filtration mechanism of Pb(II) at the surface of a clay ceramic membrane through its preconcentration at the surface of a graphite/clay composite working electrode

Lubna Jaber, Abdelaziz Elgamouz *, Abdel-Nasser Kawde *

Pure and Applied Chemistry Group, Department of Chemistry, College of Sciences, University of Sharjah, P. O. Box 27272, United Arab Emirates

Received 20 June 2022; accepted 21 September 2022
Available online 26 September 2022

KEYWORDS

Clay mineral;
Membrane;
Heavy metals;
Cyclic voltammetry;
Electrochemical surface

Abstract The use of cyclic voltammetry (CV) and linear scan anodic stripping voltammetry (LSASV) to predict the selectivity of microfiltration ceramic membranes made from a lump of local clay towards Pb(II) ions filtration is described. The membranes were characterized by different techniques followed by CV analysis of the $Fe(CN)_6^{3-}/Fe(CN)_6^{4-}$ redox couple and Pb(II) on bare graphite, raw clay, and clay-modified carbon paste electrode (clay-modified CPE). The effect of clay loading in the range of 1–10 % (w/w) on the electrodes is studied, where an enhanced peak current is observed for 5 % w/w clay. Moreover, a decrease in the peak current can be seen for bare graphite electrodes, suggesting that the clay mineral had played a substantial role in the sieving of heavy metal ions through the ceramic membrane. The electroactive surface area of 5% w/w raw clay towards Fe(II) ions was found to be in the order of 3.07×10^{-2} cm^2 and higher than 5% w/w clay sintered to 1000 °C and bare graphite. CV analysis shows that both, 5 % w/w raw clay and 5 % w/w clay sintered to 1000 °C exhibited high peak currents towards Pb(II) ions. The mobility of the Pb(II) ions is found to increase when 5% w/w clay sintered to 1000 °C is utilized as membrane/electrode, leading to an increase in the amount of reduced Pb(II) ions on the surfaces of the clay membranes/-electrodes. The study suggests successful filtration of Pb(II) ions through the proposed membrane/-electrode and a much better accumulation than Fe(II) at the surface of the membrane/electrode before being subjected to filtration.

* Corresponding authors.
E-mail addresses: U20105005@sharjah.ac.ae (L. Jaber), aelgamouz@sharjah.ac.ae (A. Elgamouz), akawde@sharjah.ac.ae (A.-N. Kawde).
Peer review under responsibility of King Saud University.

Production and hosting by Elsevier

https://doi.org/10.1016/j.arabjc.2022.104303

1. Introduction

Heavy metals' (HM) contamination arises from numerous events including anthropogenic, mining, fertilizers, and other chemicals produced from industrial or household activities, as a result of increasing global population and demand for resources (Kapoor and Singh, 2020; Mukherjee et al., 2021). Lead (Pb) is among the highly toxic heavy metals widely found in water infrastructures (Gumpu et al., 2015)–(Cui et al., 2015), considerably dangerous and extremely destructive to the environment, and hazardous to human health (Guo, 2016; Na Kim et al., 2012). Such metal ions exhibit adverse effects on the human physiology and other biological processes, even at low concentrations. Heavy metals are nonbiodegradable and tend to accumulate in living organisms, causing many diseases and dysfunctions to the nervous, immune, reproductive and gastrointestinal systems (Turdean, 2011), (Tag et al., 2007), (Afkhami et al., 2013). Therefore, it is necessary to develop a highly sensitive and selective method for the determination of toxic heavy metals in trace levels, particularly in water and biological samples.

Up until now, numerous techniques have been employed for the determination of trace heavy metals such as lead ions. Conventionally, optical techniques like spectrophotometric measurements (Aragay and Merkoçi, 2012) and spectroscopic techniques such as atomic absorption spectroscopy (AAS) (Altunay et al., 2019), inductively coupled plasma-mass spectroscopy (ICP-MS) (Choi, 2019), X-ray fluorescence (XRF) (Byers et al., 2019), neutron activation analysis (NAA) and inductively coupled plasma-optical emission spectrometry (ICP-OES) (Selmi et al., 2021) have been widely used for the detection of heavy metals in large matrices. These techniques are widely known for their high sensitivity, simultaneous elemental detection and low detection limits in the order of femtomolar (fM) range (Pujol et al., 2014). Consequently, their high cost, the need for extensive personnel training for instrument operation and multi-sample preparation make them very challenging for frequent use. Typically, these techniques are suitable for quantitative analysis and may need to be coupled with other chromatographic techniques for performing metal ion speciation (Feldmann et al., 2009). Therefore, great interest has been established in developing rapid, low cost and simple techniques suitable for HM measurements such as electrochemical techniques which are very economical, user-friendly, reliable, and suitable for many applications. Recently, many studies have been reported for the detection of Pb (II) ions using various electrochemical techniques and electrode materials due to their low cost, simplicity, rapidness, lower sensitivity, and detection limits as compared with conventional methods. For instance, cyclic voltammetry (CV) electrochemical technique is considerably known for its versatile applications in a vast majority of areas. Data collected from cyclic voltammograms (CVs) are very useful in fulfilling the work and thus provides essential information about the structure, potential and characteristic activities. Additionally, CV gives an insight on the mechanism of electron transfer reactions along with their quantitative and synthetic relevance in order to evaluate the behavior of target substances and thus support their characterizations (Chooto, 2019).

Many studies have reported various approaches for modifying the surface of the working electrode for Pb(II) detection (Mohammed et al., 2022), (Huo et al., 2022), (Wang et al., 2022), (Hashemi et al., 2022), (Bodkhe, 2021). Among them include naturally occurring materials such as clays that are primarily constituted from silicate and alumina. Their wide range of occurrences and availability has made them a subject of many studies (Ito and Wagai, 2017). Recent trends of interest in clays are based on the internal properties induced by the laminar structures that are formed from the sequence of silicon tetrahedral and aluminum octahedral layers. The interlayer confined spaces can be used as an internal cavity to encapsulate guest analytes by isolating them from the bulk and inducing specific conformation on them (Veerabadran et al., 2008). Separation based on membrane techniques is one of the most efficient techniques that are limited by thermodynamic equilibriums whereas the membrane design is limited by the mass that could be transferred through the membrane. Ultrafiltration (UF), microfiltration (MF), nanofiltration (NF) and reverse osmosis (RO) account for the majority of separation techniques used in membrane separation (Khemakhem et al., 2017). Ceramic membranes are a class of membranes made from different materials such as fibers, interconnected metallic rods, alumina, and clays that can work in extreme conditions such as high pH and high temperatures (Elgamouz and Tijani, 2018). They can be produced by compaction process, sol–gel methods (Samain, 2014), extrusion (Fan et al., 2016), and hydrothermal synthesis (Wang, 2012). Compaction technique is frequently used for fabricating porous ceramics as compared to other techniques (Mouiya, 2017; Stawiski, 2014). The incorporation of clay materials in the fabrication of membrane is based on the fact that clays can be plasticized when mixed with water and could be compacted without using additional binders. Further, the selection of clay materials is mainly accounted for their environmental friendliness, cost, and availability. These materials are incontestably better than synthetic materials that may present a high risk to the environment (Aboudi Mana et al., 2017). Different clays from different origins worldwide have been used for the preparation of clay supports (Elgamouz and Tijani, 2018; Alves Xavier et al., 2019), (Mouiya et al., 2019), (Elgamouz and Tijani, 2018), (Elgamouz et al., 2020), (El-Kordy et al., 2022), (Lahnafi et al., 2022), (Elgamouz et al., 2019). Many transport mechanisms have been proposed for separation of heavy metals using membranes namely size exclusion, adsorption, and polarity of the permeant towards the membrane (Saleh and Gupta, 2016). Zeta potential and point of zero charge are among the widely used techniques to study the polarity rejection mechanism. For example, RoyChoudhury *et al.* (RoyChoudhury et al., 2019) demonstrated that the point of zero charge of hydroxyapatite (HAp) based Alumina-Clay-ceramic membrane was found to be at pH = 2.2. During the filtration of Pb(II), the surface of the membrane was found to be negatively charged since pH of HAp suspension is above 2.2. The elimination of Pb(II) ion was explained based on electrostatic repulsion between the negatively charged membrane and the positively charged cation. The size exclusion theory was excluded in this study. However, a polyamide membrane assembled directly on a kaolin substrate (KS-PSL) constituting of an acceptable pore size allowing the passage of molecules between 260 and 314 Da in size was prepared by Zhou *et al.* (Zhou et al., 2022). In this study, the effective membrane was found to retain relatively large hydrated Pb(II) and Cd(II) ions through size exclusion effect. Meanwhile, when the polyamide is assembled on the Al_2O_3/Carbon Black nanolayers (KS-PNI), zeta potential was used to explain the mechanism of filtration of the KS-PNI membrane, at pH less than 5.0, and due to presence of amine functional groups on its surface, the KS-PNI membrane is presented with a positive surface potential repelling the nitrate anions, hence electropositive nitrate counter anions (Pb(II) and Cd (II)) stay in the feed solution to counter balance the negative charge of the nitrate anions. Zeta potential is widely used to study the repelling mechanisms of filtration of many charged species. However, it is not appropriately estimated. Zeta potential is assessed in the presence of different concentration of H^+ (pH dependent) not the analyte species. In the present study, the use of electrochemical techniques is proposed to foresee the selectivity of MF ceramic membranes made from a lump of local clay sampled from the United Arab Emirates (UAE) as an effective material for Pb(II) ions retention. The paper reports the preparation and characterization of clay-modified CPE, prepared by compaction and sintering technique from temperatures between 250 °C and 1100 °C representing the ceramic membrane used for the filtration of Pb(II). The electrochemical performance of clay-modified carbon paste membrane/electrode is evaluated against bare graphite reference electrode and raw clay, exhibiting markedly high peak currents in the presence of Fe (II) and Pb(II) metal ions.

2. Materials and methods

2.1. Clay sampling

The clay material investigated in this study was collected from Wadi Haqil Ras Al-Khaimah, UAE. The sampling site is situated approximately 3.0 km from Ras Al-Khaimah town center (Geographical coordinates: Latitude: 25°48′46″ North and the Longitude: 56°2′54″ Est). The clay material was pulverized manually with a mortar then different granule sizes were obtained using ASTM (American Society for Testing and Materials) standardized sieves. Approximately, 5 sizes were collected by mounting the sieves on top of each other. The fraction size in the range of 250–425 μm was used in the fabrication of the clay membrane supports.

2.2. Reagents

All chemicals were of analytical reagent grade and were used without further purification. Lead(II) nitrate ($Pb(NO_3)_2$, ACS reagent, ≥99.0 %), potassium chloride (KCl, ACS reagent, ≥99.0 %), Potassium hexacyanoferrate (II) trihydrate ($K_4Fe(CN)_6{\cdot}3H_2O$, ReagentPlus, ≥98.5 %), hydrochloric acid (HCl, 37 %), graphite powder (20 μm, synthetic), mineral oil, phosphate-buffered saline (PBS, pH = 5,7) and boric acid/potassium chloride/sodium hydroxide buffer solution (pH = 10) were purchased from Sigma Aldrich. Activated carbon (sieved over 40 × 40 mesh, loss on ignition: 10 % at 120 °C and residue on ignition: 7 % at 800 °C) used as a porosity promotor was purchased from Fisher Scientific. Acetate buffer solution (0.1 M, pH 4.5) was prepared from sodium acetate (CH_3COONa) and acetic acid (CH_3COOH). The pH of the buffer solution was then adjusted using HCl. Deionized water (resistance = 15.0 MΩ.cm) was used throughout the experiments and for the preparation of solutions obtained from Elix® Essential 5 deionizer.

2.3. Clay membranes preparation

Clay mineral was sampled from the northern region of the United Arab Emirates. Particles ranging in size between 250 and 425 μm were made using ASTM standardized sieves. In brief, 3.0 g of 3 % (w/w) (activated carbon/clay) were shacked thoroughly to assure proper homogeneity, then introduced into a stainless-steel die set and pressed under 518 bar of uniaxial pressure, were flat discs like pellets (30.0 mm diameter, 2.0 mm thickness) were obtained. The consolidation of the membrane is assured by the surface adsorbed and constitutional waters of the clay; therefore, no water was added to the powders. The raw flat-disc membranes were sintered to final temperatures ranging between 250 and 1100 °C, using an electric furnace (CARBOLITE type 11/6B) following a heating program developed based on physicochemical phenomena occurring in common clay minerals based on thermal analysis. Clay membranes are crushed and ground into fine powders for further use in thermogravimetric analysis (TGA), X-ray fluorescence (XRF), X-ray diffraction (XRD), Fourier Transform Infrared Spectroscopy (FTIR), Scanning Electron microscopy equipped with Energy Disperse Spectroscopy (SEM/EDS) and for the preparation of electrochemical sensors.

2.4. Clay fraction isolation

5.0 g of ground clay was suspended in 1.0 L of deionized water and stirred for 18 h. 10.0 % HCl solution was added dropwise to the suspension with a speed of 2 drops/hour, where a total number of 50 drops were added resulting in the final pH of the suspension of 7.30. At this stage, the suspension was allowed to settle for 50 min. 40.0 mL aliquot of the supernatant was placed in four test tubes and centrifuged at 2700 rpm for 30 min. A very small amount of solid was recovered from the bottom of each tube and combined in one test tube then centrifuged again at 1750 rpm for 30 min. The recovered solid was then collected for XRD analysis. The analyzed sample was not identified as the clay fraction. The rest of the supernatant in the 1.0 L beaker was discarded and the settled coarse material at the bottom of the beaker was collected in 80.0 mL deionized water then transferred to test tubes and centrifuged at 3500 rpm for 40 min. The supernatants were discarded, and solids were suspended again in water and centrifuged at 600 rpm for 7 min, this operation was carried out two times to wash the solid material. At the final step, the cloudy supernatant was suspected to contain particles with a size less than 2 μm (clay fraction), which was then collected in a 100 mL beaker and further centrifuged at 2750 rpm for 40 min. Finally, the solid collected from the test tubes was analyzed in the XRD machine.

2.5. Characterization of clay ceramic membranes

Flat disc ceramic membrane supports prepared and sintered at different final temperatures were weighed then inserted in a beaker of water and left for a period of 48 h. Final masses of the support were recorded after being removed from the water and air dried for 2 h. The porosity of clay supports was calculated using Eq. 1.

$$P\% = \left(\frac{m_f - m_i}{m_i}\right) x100 \quad (1)$$

where m_i and m_f is the initial and final mass of the support.

Structural characterization of the clay ceramics membranes is performed by TGA, XRF, XRD, FTIR, and morphological study by SEM/EDS. Thermal analysis is performed using NETZSCH STA 449 F5 Jupiter operating in TGA modes under air at a linear static mode from room temperature of 25 °C to a final temperature of 1200 °C with a heating rate of 20 °C/min. XRF analysis is used to determine the chemical composition of the raw and sintered clay samples. A Philip model PW 1410 XRF machine with chromium target, PE crystal (2d = 8.742 Å) analyzer, and gas flow proportional counter was used. The tube rating was 50 kV, 40 mA, and 2θ range of 58° to 147°. The 2θ range is found to be suitable for major elements determination in clay using a recorder coupled detector. XRD was performed on the isolated clay fractions obtained using the process detailed above as well as raw and sintered clay materials to study the extent of phase transformations. Diffraction patterns were obtained with CuKα radiation (λ = 1.540 Å) on a PW1710 Philips Analytical diffractometer controlled by XPERT Quantify software (EA Almelo, The Netherlands) operating at 40 kV and 30 mA, with a copper anode and a graphite monochromator. The data was collected between 2θ = 5.0° to 85° in incremental steps of 0.05° with a

rate (t) = 0.5 s/step. A monochromator with a normal divergence (1.0°) and receiving slits of 0.1 mm dimensions were used. 1300 points were recorded using continuous scans. Non-oriented preparations of the samples were used; fine powders were used in order to ensure the homogeneity of the sample. This method is very reliable and gives excellent results with regard to the total recovery of the clay mineral. The powder sample consisted of a given crystalline phase that always gave rise to diffraction peaks in the same directions, with relatively constant heights. This diffraction pattern thus formed a true signature of the clayey phase. FTIR of the clay materials was recorded using an FT-IR JASCO 6300 Spectrometer fitted with an attenuated total reflection (ATR) unit, with single reflection geometry. The clay material powders were kept at 70 °C in an oven, then taken in a desiccator for FTIR (ATR) analysis. Samples were introduced to the ATR unit with a single reflection geometry and spectra were collected in the range 4000–400 cm^{-1} in the transmittance mode after 31 scans. The morphology and composition of the clay material were visualized and analyzed using a ThermoFisher Scientific Apreo C FESEM equipped with an EDS detector to examine the abundance of elements, presence of possible structural defects, and estimated membrane pore size. SEM micrographs were taken at an accelerating voltage of 20 kV.

2.6. Electrochemical techniques to study membranes selectivity

CV and LSASV of Fe(II) and Pb(II) on the surface of the clay-modified CPE are performed to study the selectivity of clay ceramic membranes. Carbon paste membranes/electrodes are fabricated by mixing graphite powder, clay membrane, and mineral oil serving as a binder of the paste. To ensure homogeneous and uniform mixing, the paste is mixed for a period of 10–15 min using a glass rod. The uniformly obtained pastes are then loaded into the sensing part of a 3D printed working electrode body with dimensions identical to the commercial glassy carbon electrode (7.0 cm long, 2.0 mm diameter) using a copper wire as an electric contact. Prior to any experiment, a new paste is loaded to the sensing part of the electrode and the sensing surface is smoothed on a wax paper. The bare graphite paste is prepared in the same way, without the addition of clay membrane powder, and is utilized for reference responses' comparison. Table 1 presents the preparation of various ratios of composite membranes/electrodes with graphite powder, ceramic clay, and mineral oil ranging from 1 to 10 wt%. Electrochemical measurements are recorded on a Zahner Ennium Pro 43,243 electrochemical workstation. The electrochemical cell contained a clay-modified carbon paste membrane/electrode as a working electrode, a Pt wire counter electrode, and an Ag/AgCl (Sat. KCl) as a reference electrode.

Table 1 The composition ratio of the prepared electrodes.

Sample	Graphite (wt.%)	Clay (wt.%)	Mineral oil (wt.%)
Graphite	70	0	30
1 % clay	69	1	30
3 % clay	67	3	30
5 % clay	65	5	30
10 % clay	60	10	30

3. Results and discussion

3.1. Characterization of clay ceramic membranes

The porosity of the flat membrane discs sintered to 800, 900, 1000 and 1100 °C was measured using the conventional Archimedes technique (Lahnafi et al., 2020) and the results are tabulated in Table S1. The membrane discs sintered to temperatures below 800 °C were very weak, therefore they were not suitable for water porosity measurements. At higher sintering temperatures, the porosity of the membranes was found to decrease, indicating that the clay is better consolidated, developing better mechanical and chemical strength making the membranes more suitable for filtration in drastic conditions. Porosity values of 10.06 ± 1.56 %, 7.75 ± 1.61 %, 4.14 ± 0.74 % and 2.70 ± 0.40 % were found for the discs sintered to 800, 900, 1000 and 1100 °C, respectively. The membranes sintered to 1000 °C were presented with the best mechanical strength and appropriate porosity as demonstrated in a previous study (Elgamouz et al., 2019). Therefore, membranes sintered to 1000 °C were further investigated for the study of Pb(II) filtration using CV and LSASV.

Thermal analysis using TGA was performed on raw clay material to identify the temperature regimes at which drastic weight losses and possible phase transformations take place. The study provided insight into the effect of various temperature regimes on the porous structure and pore diameter of the membrane. Fig. 1 displays the TGA curve of raw UAE clay material when subjected to heat from 25 to 1200 °C in an alumina crucible at a heating rate of 20 °C/min. The figure clearly shows existing complex phase transformation and interactions. The total weight loss of the sample is observed to be 17.84 %. The process could be divided into five steps. The first mass loss of 4.67 % occurring at 195 °C is attributed to the loss of water molecules. The second step observed a weight loss of approximately 2.3 % between 195 and 488 °C, which can be correlated to the pre-dehydration step of kaolin. The pre-dehydration of kaolin occurs due to the rearrangement of the octahedral layers, first occurring at the OH on the surface

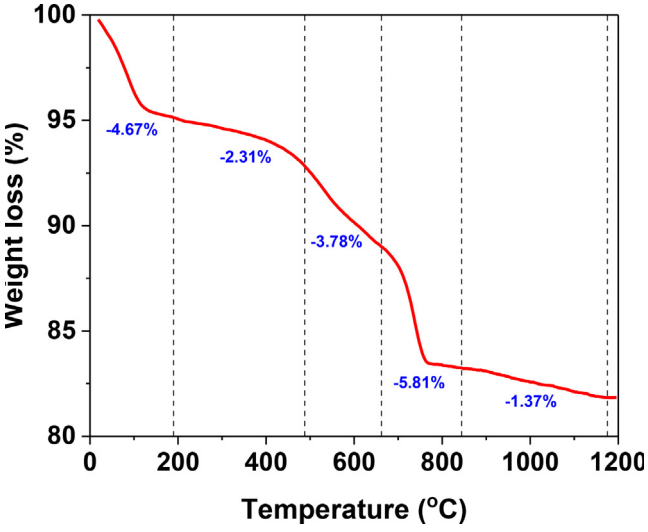

Fig. 1 Thermal gravimetric analysis of the raw clay material used in the preparation of the clay membranes.

(Balek and Murat, 1996). Between 488 and 662 °C, the loss of hydroxyl groups takes place due to the transformation of kaolinite to metakaolinite according to the following chemical reaction (Chen et al., 2004).

$$Al_2O_3.2SiO_2{\cdot}2H_2O(\text{kaolinite}) \rightarrow Al_2O_3.2SiO_2(\text{metakaolinite}) + 2H_2O \quad (1)$$

The calcination of $CaCO_3$ resulted in the production of CO_2 and therefore the improvement of the porous membrane structure within the temperature regime of 662 °C to 849 °C, corresponding to a total weight loss of 5.81 %. Lastly, the calcination of Na_2CO_3 corresponds to a very minimal loss of mass above 849 °C.

The chemical composition of the raw and sintered clay at 1000 °C samples obtained from the XRF are presented in Table 2. The loss on ignition (LOI) is calculated at 800 °C for the raw clay, while sintered LOI presents the weight difference between the sintered clay at 800 °C and 1000 °C. Alumina, silica, iron, and calcium oxides were found to be the major components of the two samples. These are followed by magnesium oxide and traces of titanium and manganese oxides. Changes in the oxides percent were recorded when the clay is sintered to 1000 °C, indicating the rearrangement of the inorganic phases present in the clay. For instance, iron is known to change its oxidation state from Fe(II) to Fe(III). While loss on ignition for raw clay was in the range of 17.50 ± 0.24 %, this loss is due to phase change, mass loss, and iron oxide transformation (Elgamouz et al., 2019). Mass loss for the sintered sample at 1000 °C was recorded in the order of 0.53 ± 0.05, indicating that the carbonaceous compounds had been removed at lower sintering temperatures.

Fig. 2 summarizes XRD patterns of raw and sintered clay at 250 °C, 500 °C, 700 °C, 1000 °C and 1100 °C for 2 h in a muffle furnace. The XRD patterns of raw clay fraction presented in Fig. 2A indicate that the inorganic mixture originally consists of illite, smectite, and kaolinite minerals in the clay sample. Based on Fig. 2B, the XRD trends show no significant changes to kaolinite in the clay structure, however with increasing sintering temperatures, calcium carbonate, and quartz peaks diminish above 700 °C. This suggests that these materials either melt into the clay matrix or a phase conversion from kaolinite to metakaolinite takes place as illustrated by the TGA curves. The other existing phases that appear are quartz and chlorite. As a result of no further significant phase transformation occurring at higher temperatures, this implies that the clay ceramic membrane skeletal structure constitutes mainly metakaolinite, quartz, smectite, illite, and chlorite.

FTIR spectroscopy is used to analyze the composition/-functional property of raw clay and sintered clay in an acquired range of 400–4000 cm^{-1} and results are shown in Fig. 3A-C and tabulated in Table S2 (supporting document). The band at 3474 cm^{-1} may correspond to the Al----O—H stretching mode of clay mineral (Kaolinite). Vibration peaks at 1733 and 1654 cm^{-1} can be attributed to C═O stretching and H—O—H bending of water molecules which are adsorbed on the surface of the clay, respectively. The small bands at 1449 cm^{-1} can be ascribed as C—H bending. The peak vibrations at 1373 and 992 cm^{-1} can be attributed to Al-O and Si-O stretching vibrations of the clay mineral (Kaolinite). The absorption band at 1211 cm^{-1} represents the stretching vibration of C—O of organic matter present in the clay mate-

Table 2 The clay oxides' composition obtained from XRF analysis.

Sample	SiO_2	Al_2O_3	Fe_2O_3	CaO	MgO	K_2O	TiO_2	MnO_2	LOI
Raw clay	47.08 ± 0.58	10.67 ± 0.48	17.61 ± 0.20	14.07 ± 0.34	6.37 ± 0.35	1.99 ± 0.07	1.38 ± 0.01	0.36 ± 0.03	17.50 ± 0.24
Sintered clay	45.77 ± 0.51	9.94 ± 0.37	18.38 ± 0.43	15.48 ± 0.14	5.91 ± 0.30	1.91 ± 0.03	1.46 ± 0.03	0.39 ± 0.02	0.53 ± 0.05

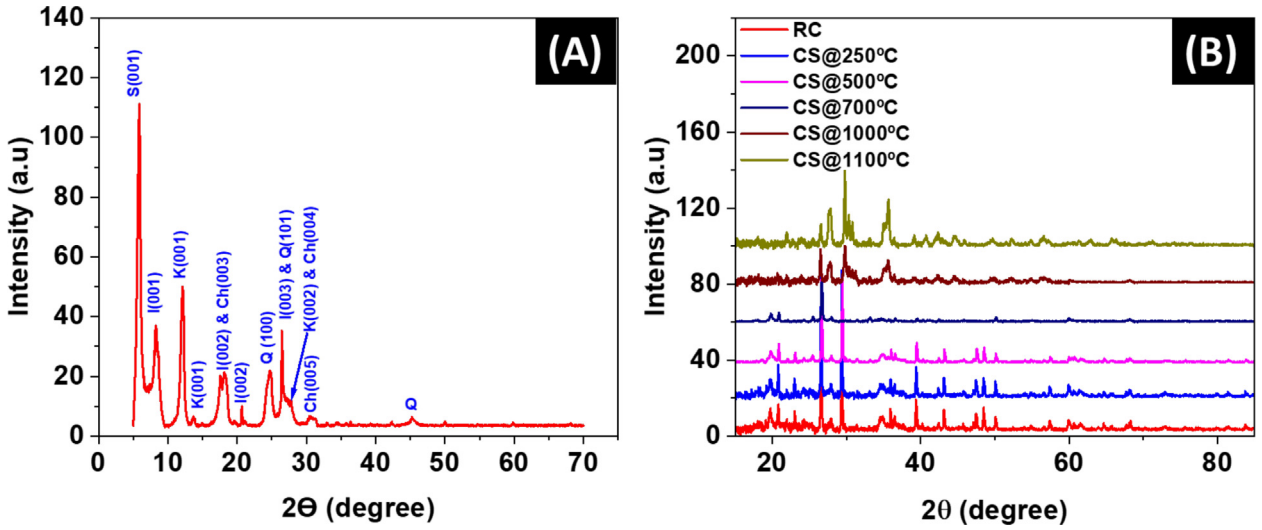

Fig. 2 XRD pattern of (A) Raw UAE clay fraction and (B) Raw clay (RC) and clay sintered (CS) to various temperatures of 250 °C, 500 °C, 700 °C, 1000 °C, and 1100 °C. Abbreviations; I: illite; K: Kaolinite; Q: quartz; S: smectite; Ch: Chlorite.

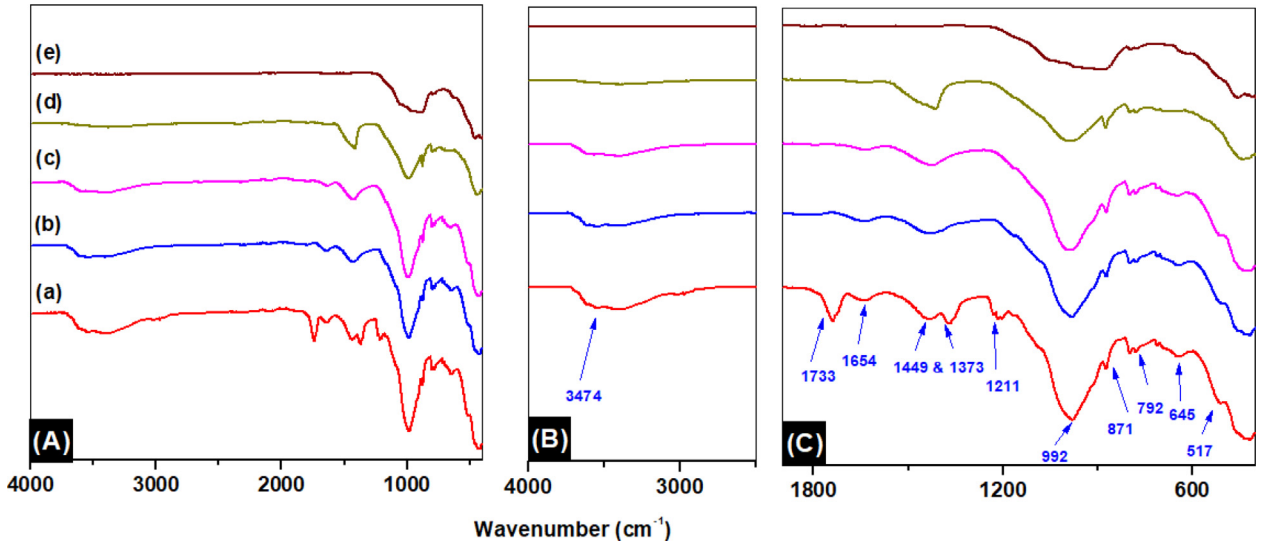

Fig. 3 FT IR spectra of (A) overlay spectra of (a) RC, (b) cCS@250 °C, (c) CS@500 °C, (d) CS@700 °C, (e) clay CS@1000 °C and (f) CS@1100 °C, (B) zoom-in of 4000–2500 cm^{-1} and (C) zoom-in of 4000–400 cm^{-1}.

rial, which is seen to disappear after the sintering process (Zuo et al., 2018; Akanji et al., 2019). Peaks at 871 and 792 cm^{-1} may be corroborated by the OH deformation linked to $2Al^{3+}$ and Si-O quartz, respectively. Furthermore, vibration peaks appearing at 645 and 517 cm^{-1} can be correlated to Si-O-Si bending.

Fig. 4 (A-D) displays the SEM images of raw clay and clays sintered at 250 °C, 1000 °C, and 1100 °C. The clay samples showed a surface with a rough morphological structure. It was also noticed that the membrane porosity decreased for the sintered clay and the grains become fused. The more consolidated membrane structure is a result of particles agglomeration, creating a denser ceramic body. The observed SEM images signify that the membrane did not have any pinholes cracks, making the membrane suitable for the microfiltration application. SEM micrographs of clay modified carbon paste membranes/electrodes presented in Fig. S1 (supplementary document) show difference in the morphology in comparison with the unmodified surfaces. The figure shows increased pore sizes and uneven distribution of the pores on the modified surface. Furthermore, Table S3 (supporting document) represents the atomic composition of powdered and paste materials for raw clay and clays sintered at 250 °C, 1000 °C, and 1100 °C. The prepared materials demonstrate the presence of O, Si, C, Al, Fe, Ca, Mg, and traces of Mg and K in clay mineral powders whereas excessive amounts of C (≥95 %) was observed in 5 % clay modified carbon paste materials.

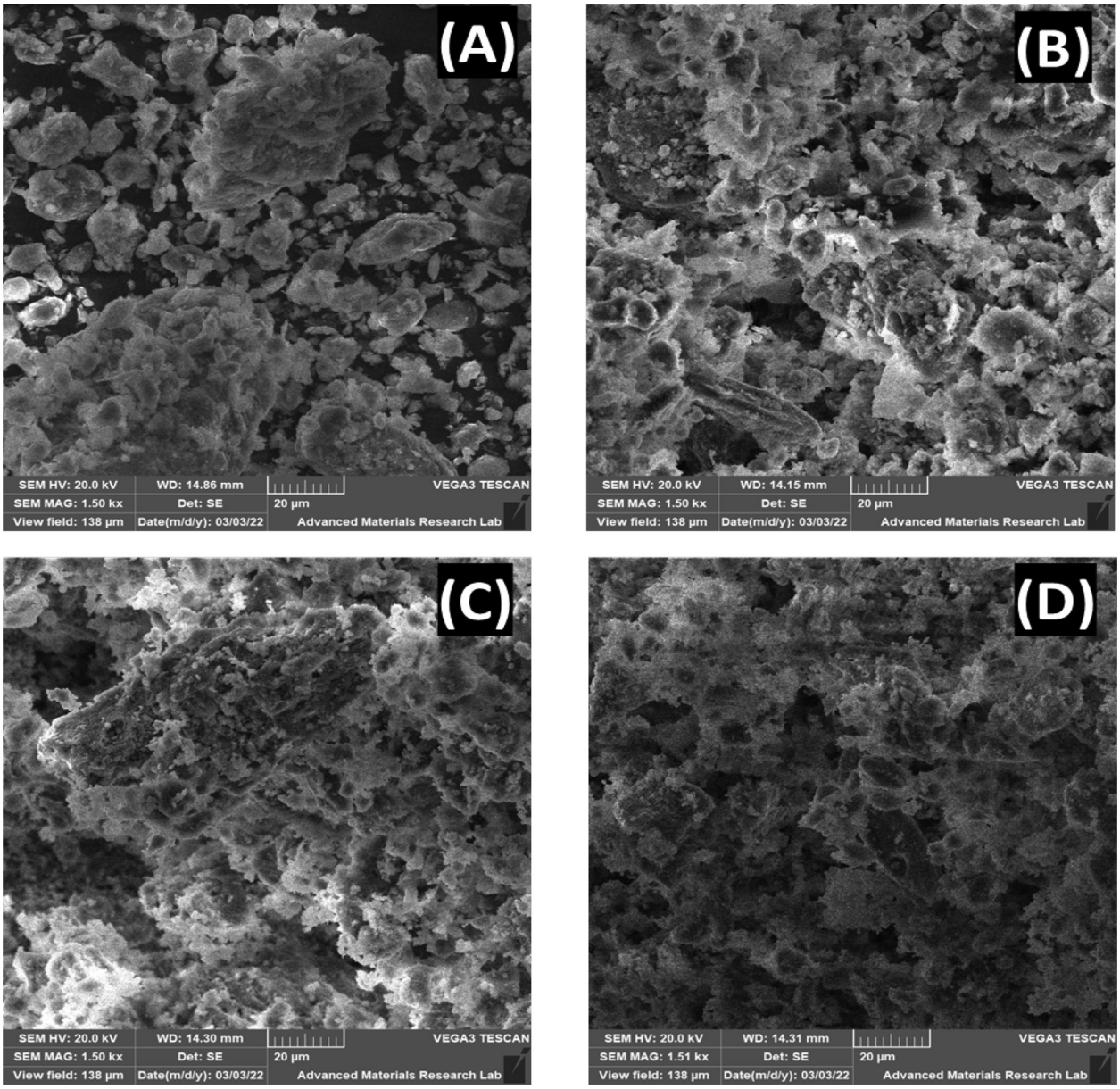

Fig. 4 SEM micrographs of (A) RC, (B) CS@250 °C, (C) CS@1000 °C, (D) CS@1100 °C.

3.2. Electrochemical experiments

3.2.1. Effect of GR and GR/clay mass ratio

CV was employed to evaluate the electrochemical properties of the bare graphite and clay-modified CPE with different clay loadings (wt.%), where 10 mM $K_4Fe(CN)_6$ and 0.1 M KCl were used as the electroactive species and supporting electrolyte, respectively. The analysis was carried out at a potential range between 750 mV and −300 mV; current ranging between −500 mA and 500 mA and a scan rate of 100 mVs^{-1}. The CVs presented in Fig. 5 show well-defined oxidation and reduction peaks and an enhanced peak current at 0.25 V with increase in electron transfer kinetics with 5 wt% clay composite compared to 1, 3, and 10 wt% clay composite and bare graphite. This validated significant changes in the electrode surface property and showed good electrocatalytic activity of the modified electrodes towards $K_4Fe(CN)_6$. Hence, all further studies were carried out using a 5 wt% clay composite electrode as the optimum clay loading.

3.2.2. Effect of scan rate

Fig. S2 (supporting document) shows the influence of scan rate on the CV peak currents of the $Fe(CN)_6^{3-}/Fe(CN)_6^{4-}$ redox couple in the scan rate range of 5 to 200 mVs^{-1} for 5 % raw and sintered clay composite membranes/electrodes. Initially, CV analysis of bare graphite, 5 % raw clay, and 5 % clay sintered to 250℃, 500℃, 700℃, 1000℃, and 1100℃ were conducted at different scan rates in the presence of 10 mM $K_4Fe(CN)_6$ and 0.1 M KCl to examine the electroactive surface area of each membrane/electrode. Reproducible anodic and cathodic peaks were obtained owing to $Fe(CN)_6^{3-}/Fe(CN)_6^{4-}$ redox couple at the membrane/electrode surface. The electroactive

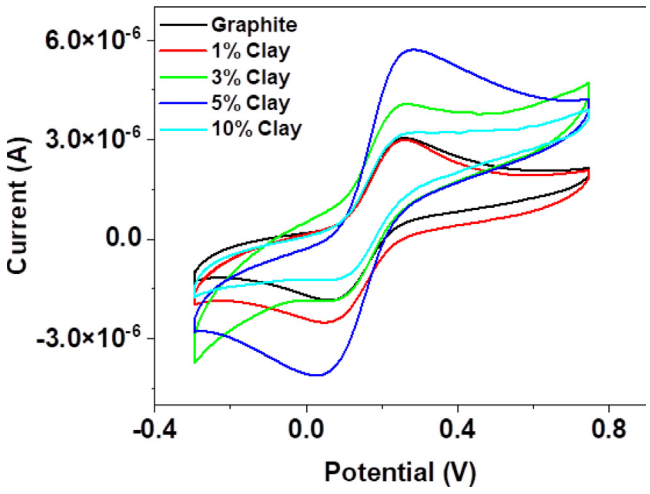

Fig. 5 CVs in the presence of 10 mM $K_4Fe(CN)_6$ solution at a scan rate of 100 mVs^{-1} for GR and GR/Clay mass ratio optimization.

surface areas of the membranes/electrodes are calculated by applying the Randles-Sevcik equation (2) (Moudam and El Gamouz, 2016).

$$I_p = 2.69 \times 10^5 n^{\frac{3}{2}} A D^{\frac{1}{2}} C \gamma^{\frac{1}{2}} \quad (2)$$

where C is the concentration of the analyte ($molL^{-1}$), n is the number of electrons that contribute to the redox reaction on the membrane/electrode surface, A is the electroactive surface area of the membrane/electrode (cm^2), D is the diffusion coefficient ($cm^2\ s^{-1}$), and γ is the scan rate (Vs^{-1}). With the aid of the CVs presented in Fig. S2 (supporting document), the electroactive surface areas were calculated, then displayed as a bar graph in Fig. 6 and tabulated in Table 3.

The linear increase of the cathodic peak current versus the square root of the scan rate indicates that the diffusion of Fe

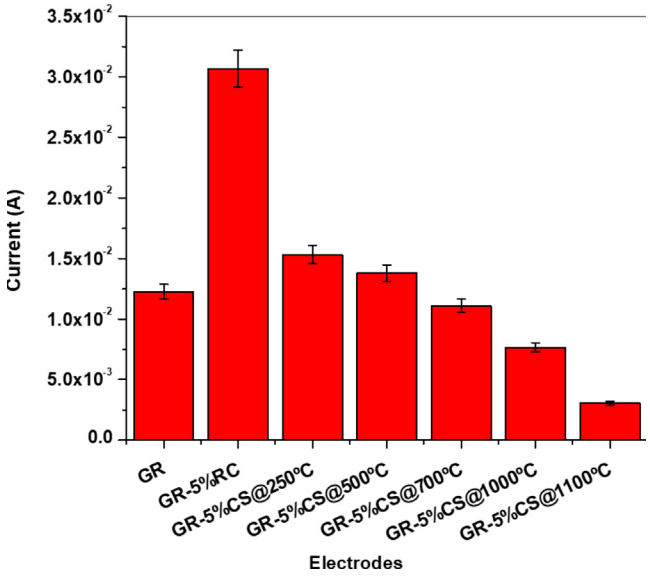

Fig. 6 Bar graph representing the calculated electroactive surface areas of different carbon paste membranes/electrodes using Randles-Sevcik equation.

Table 3 The calculated electroactive surface area of each carbon paste membrane/electrode evaluated at different scan rates.

Electrode	Composition	Electroactive surface Area (cm^2)
GR	Bare graphite	1.23×10^{-2}
GR-5 %RC	5 % raw clay	3.07×10^{-2}
GR-5 % CS@250 °C	5 % clay sintered to 250 °C	1.53×10^{-2}
GR-5 % CS@500 °C	5 % clay sintered to 500 °C	1.38×10^{-2}
GR-5 % CS@700 °C	5 % clay sintered to 700 °C	1.11×10^{-2}
GR-5 % CS@1000 °C	5 % clay sintered to 1000 °C	7.67×10^{-3}
GR-5 % CS@1100 °C	5 % clay sintered to 1100 °C	3.07×10^{-3}

$(CN)_6^{3-}/Fe(CN)_6^{4-}$ redox couple on the membrane/electrode surface took place (Raghavendra, 2021; Moutcine, 2020). In addition, a decrease in the electroactive surface of the membrane/electrode with increasing sintering temperature was noticed. This behavior can be explained by the decreased membrane porosity for the sintered clay and fusion of the grains. At higher sintering temperatures, the membrane becomes more consolidated due to particle agglomeration, generating a denser ceramic body and thus decreasing the electroactive area of the membrane/electrode surface. Hence, GR-5 %CS@1000 °C membrane/electrode was selected as the optimal membrane/electrode for subsequent studies.

3.2.3. Effect of supporting electrolyte and pH on Pb(II) ions filtration

The influence of various supporting electrolytes and pHs on Pb (II) ions filtration was evaluated using GR-5 %CS@1000 °C via a LSASV. A 0.1 M concentration of different supporting electrolyte such as HCl, acetate buffer, PBS buffer and boric acid/potassium chloride/sodium hydroxide buffer was used to investigate the effect of supporting electrolyte on the filtration of Pb(II) ions on the membrane/electrode surface. The pH of the medium was varied from 1.5 to 10.0 as shown in Fig. 7A and 7B. The high peak current at low pHs could be attributed to the presence of ionized Pb(II) species and charge carriers, large enough to increase the current. In acetate buffer at pH = 4.5, the decrease in the current could be due to the hydrolysis of the metal ions. During the hydrolysis process, hydroxide ions are produced which react with the metal ions to give the $Pb(OH)^+$ species. At higher pHs (> 7), the $Pb(OH)^+$ species continue to react to give the precipitates $Pb(OH)_2$, causing little or no accumulation of Pb(II) ions by LSASV. Later, the $Pb(OH)_3^-$ anions are generated. It is also worth noting that at this extent both the GR-5 %CS@1000 °C membrane/electrode surface as well as the hydroxides hold an overall negative charge, triggering electrostatic repulsion and causing lack of interaction between the clay minerals and the Pb(II) ions. Similar results were reported in previous studies (Akanji et al., 2019; Blaise, 2022; Ns et al., 2018). Moreover, based on these outcomes, 0.1 M acetate buffer at pH 4.5 was selected an optimal supporting medium and pH for further studies. This is

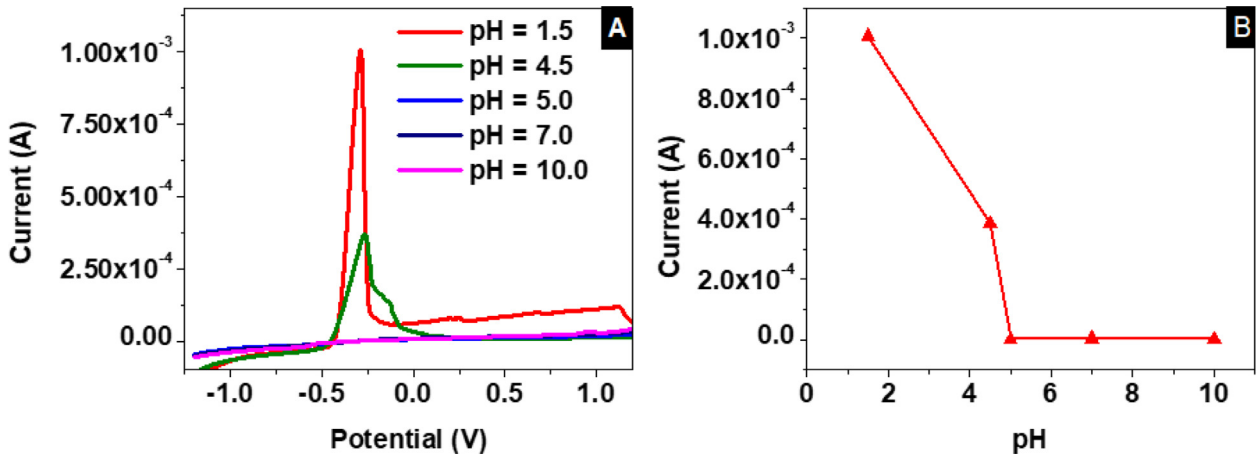

Fig. 7 The effect of supporting electrolyte and pH on the filtration of Pb(II) ions using GR-5 %CS@1000 °C via LSASV (A), and peak current of Pb(II) ions at different pH (B), at accumulation time 60 s, accumulation potential −1.2 V and scan rate of 100 mVs^{-1}.

explained by the destruction of the membrane/electrode surface at acidic mediums despite the high peak current responses and the precipitation of Pb(II) ions under basic conditions.

3.2.4. Selectivity measurements via LSASV

Additional scan rate optimization studies were conducted with 5 % RC and GR-5 %CS@1000 °C in the presence of 1.0 mM Pb(II) in 0.1 M acetate buffer of pH = 4.5 as the target analyte and supporting electrolyte, respectively. The CVs of both 5 % RC and GR-5 %CS@1000 °C represented in Fig. 8A and 8B show clear peak current consistency with increasing scan rates. The existence of an anodic peak at −0.5 V affirmed the filtration of Pb(II) ions in the system. A slight shift in the potential was observed with an increasing scan rate from −0.5 V at 5 mVs^{-1} to −0.4 V at 100 mVs^{-1}. Typically, the change in peak potentials with faster scan rates in irreversible waves usually gives information about the nature of the electron transfer, such that more potential is needed to induce the electron transfer when the electron rate constant is slow. With increasing scan rates from 5 to 100 mVs^{-1}, the concentration gradient takes longer time to react to the changes in the potential, causing the maximum concentration gradient to take place at potentials further from the initial potential at 5 mVs^{-1}. Another study reported that, the potential shift in the forward direction at fast scan rates is mainly attributed to the behavior of the heterogeneous kinetic control (Aoki et al., 2020). Moreover, a positive linear relationship was exhibited when plotting the anodic peak currents against the square root of the scan rates with R^2 values of 0.9927 and 0.9975 for 5 % RC and GR-5 %CS@1000 °C, respectively (Fig. 8C).

To further understand the selectivity of the membrane towards Pb(II), the GR-5 %RC and the GR-5 % CS@1000 °C electroactive surface areas were determined at scan rates spanning between 5 and 200 mVs^{-1}, using the Randles-Sevcik equation (1). The Pb(II) diffusion coefficient value used was 9.45×10^{-6} cm^2 s^{-1} (Sato et al., 1975). The GR-5 %CS@1000 °C was presented with higher electroactive surface area of 2.03×10^{-2} cm^2 towards Pb(II), as compared to GR-5 %CS@1000 °C electroactive surface area of 7.67×10^{-3} cm^2, obtained by using the $Fe(CN)_6^{3-}/Fe(CN)_6^{4-}$ redox couple. The significant enhancement of GR-5 %CS@1000 °C electrochemical surface area towards Pb(II) is mainly due to doping of GR with sintered membrane at 1000 °C (CS@1000 °C). This is due to the fact that at higher sintering temperatures, some of the clay mineral structures are changed and destroyed, creating a more consolidated and denser form of the membrane support. The fusion of the grains at this temperature plays a role in the selectivity of Pb(II) and Fe(II)/Fe(III) ions, such that GR-5 %CS@1000 °C is more selectivity towards Pb (II) ions than Fe(II)/Fe(III) ions. Another study reported that the hydrated radii, the hydration enthalpy of the cations as well as the space requirements in the pores of the clay minerals play a role in the selectivity order. It was reported that the high selectivity of Pb(II) ions compared to Fe(II)/Fe(III) ions is due to their complex formation with water molecules, such that Fe (II)/Fe(III) ions are more likely to form octahedral complexes, making them difficult to pass through the consolidated membrane support (Inglezakis et al., 2003).

The Pb(II) ions selectivity was further investigated by linear scan anodic stripping voltammetry. Voltammograms of Pb(II) obtained from GR, GR-5 %RC, GR-5 %CS@250 °C, GR-5 %CS@500 °C, GR-5 %CS@700 °C,GR-5 %CS@1000 °C and GR-5 %CS@1100 °C membranes/electrodes immersed in 1.0 mM $Pb(NO_3)_2$ in 0.1 M acetate buffer solution of pH = 4.5 as a function of accumulation potential are shown in Fig. 8D. An accumulation time of 60 s, accumulation potential of −1.2 V and scan rate of 100 mVs^{-1} were used. It can be seen that the stripping peak of Pb(II) was the highest with GR-5 %CS@1000 °C. The mobility of the Pb(II) ions is found to increase when 5 % clay sintered to 1000 °C was utilized as the membrane/electrode, leading to an increase in the amount of reduced Pb(II) ions on the surfaces of the clay membrane/electrode. However, a drastic decrease in the peak current is observed using 5 % clay sintered to 1100 °C. This electrochemical behavior is confirmed by the increased stripping peak currents of Pb(II) in Fig. 8D.

3.2.5. Comparative study

Table 4 shows various modified electrodes and techniques used for the detection of Pb(II) ions in water in comparison to our proposed membrane/electrode (GR-5 %CS@1000 °C). As seen from the table, majority of the studies used square wave anodic stripping voltammetry (SWASV) and differential pulse

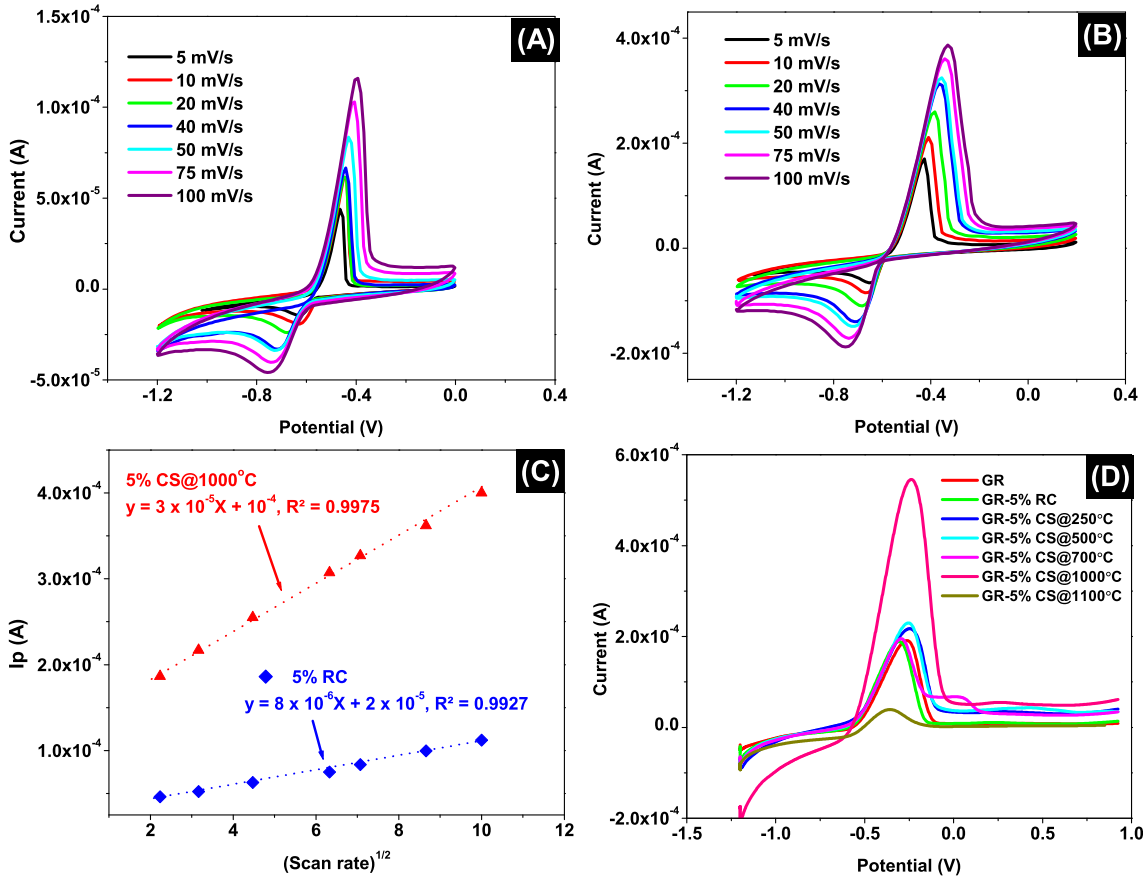

Fig. 8 Effect of scan rate on 1.0 mM ($Pb(NO_3)_2$ in 0.1 M acetate buffer solution at pH = 4.5 using 5 %-GR-5 %RC membrane/electrode (A), using GR-5 %CS@1000℃ (B), Correlation between anodic peak currents against the square root of the scan rates (C), and Linear scan anodic stripping voltammogram of lead using various membranes/electrodes: GR, GR-5 %RC, GR-5 % CS@250 °C, GR-5 %CS@500 °C, GR-5 %CS@700 °C, GR-5 %CS@1000 °C and GR-5 %CS@1100 °C, at accumulation time 60 s, accumulation potential −1.2 V and scan rate of 100 mVs^{-1} (D).

anodic stripping voltammetry (DPASV) for the detection of Pb (II) ions. Although DPASV and SWASV exhibit low capacitance current and high sensitivity, LSASV is more advantageous in terms of low background current, larger peak current, and higher resolution of overlapping. The selection of low accumulation time (60 s) during the precondition step saves great amount of time and is more cost effective which is why our proposed electrodes was preconcentrated for only 60 s whereas other studies went up to 600 s.

3.2.6. Proposed filtration mechanisms

The interaction between the clay membrane and Pb(II) ions can be thoroughly explained through the chemical composition of the clay minerals evaluated by the XRD and TGA analysis and their esteemed structural arrangement of the tetrahedral and octahedral sheets bound by shared oxygen atoms. According to the XRD analysis, the minerals present in the clay material include kaolinite (1:1 type), smectite and illite (2:1 type), chlorite (3:1 type), and quartz. These minerals are classified under the category of "layer silicates" comprising of planar octahedral layer bound to tetrahedral layer (above and below) with a distinctive repeating distance between *t*-o-t layers. These are substantially known as excellent trappers of water held between layers.

The selectivity of clay ceramic membrane sintered to 1000 °C towards Pb(II) ions is mainly attributed to the presence of smectite and illite, however other existing minerals may have also participated. Smectite are known for their interlayer expansion characteristic which takes place during their swelling behavior when they are wetted. The attraction between the oxygen atoms and top and bottom tetrahedral sheet of one unit and another generates a variable space between the layers which is then occupied by Pb(II) ions and water. The expansion of the layers arises once the exchangeable Pb(II) ions and water have entered the interlayer space. Moreover, the negatively charged clay mineral binds with the positively charged Pb(II) ions and allows them to exchange in the surrounding water, hence improving the cation exchange capacity of the smectite mineral. Furthermore, although illite are non-expanding clay minerals, their tetrahedral sheets are rich in negative charges due to the existence of 20 % aluminum atoms instead of silicon atoms, holding considerable ion (isomorphic) substitution effect. It is worth mentioning that heavy metals like Pb(II) are strongly attracted to negatively charged sites on 1:1 type layer minerals as a result of the dissociation of surface hydroxyls on these clay minerals (Kumari and Mohan, 2021). According to other studies, adsorption phenomena of Pb(II) ions by clay minerals has also been reported, explained

Table 4 Comparison of various modified electrodes, technique used, experimental conditions and sensitivity for the detection of Pb (II) ions of this work with relevant literature findings.

Electrode	Technique used	Experimental Conditions				Sensitivity	Ref.
		Electrolytic medium	pH	Accumulation potential (V)	Accumulation time (s)		
CPE-GP-Dib2	SWASV	0.2 M $NaNO_3$	2.5	− 0.90	300	52.2 μA.μM^{-1}	(Pengou et al., 2021)
CPE-ACC	SWV	0.1 M Na_2SO_4	2.0	−0.545	300	-	(Blaise, 2022)
$NHAPP_{0.5}$-CA-β-CD	DPASV	0.1 M acetate buffer	5.0	−0.80	600	100.8 μA.μM^{-1}	(Tchoffo et al., 2022)
SDS-PKC	SWV	0.1 M HNO_3	–	−0.10	30	-	(Akanji et al., 2019)
CPE/2-benzimidazolethiol	SWV	0.1 mol m^{-3} Tris-HCl	4.6	−0.80	–	-	(Touzara et al., 2022)
EDTA-CPE	SWV	0.1 M tris HCl	5.06	–	420	-	(Touzara et al., 2019)
Au/SWNTs@MOF-199 GCE	DPV	0.1 M Acetate buffer	5.0	–	300	-	(Bodkhe, 2021)
pg-C3N4/CoMn2O4	SWASV	0.1 M Hac-NaAc	5.0	−0.90	180	22.39 μA. $\mu M^{-1}.cm^{-2}$	(Wang et al., 2021)
polyPCA/GE	SWASV	0.1 M Acetate buffer	4.5	−1.6	152	-	(Lima and Soares, 2021)
NiO/rGO/GCE	SWASV	0.1 M HAc-NaAc	5.0	1.0	120	92.81 μA.μM^{-1}	(Sun et al., 2019)
GR-5 %CS@1000 °C	LSASV	0.1 M Acetate buffer	4.5	−1.2	60	81.04 μA. $\mu M^{-1}.cm^{-2}$	This work

by ion exchange and hydrogen bonding mechanism with the hydroxyl groups (Blaise, 2022; Mohajeri et al., 2018; Kypritidou et al., 2017).

According to Niraka Blaise *et al.,* (Blaise, 2022), it was reported that electrostatic attractions between the Pb(II) ions and clay minerals on the surface of the electrode may be attributed to the adsorption process. The presence of oxygen atoms from the numerous metal oxide of the clay material such as Al_2O_3, Fe_2O_3, SiO_2, and CaO (Nguetnkam et al., 2005), can form coordination bonds with the electronic valency of Pb (II). Since hydrated Pb(II) ions have an ionic radius in the order of 0.426 nm (Suchet, 1960), and graphite sheets have an interfoliar distance of around 0.335 nm (Hérold and Lagrange, 2003), the Pb(II) ions are expected be trapped in the interfoliar spaces of clay and graphite during adsorption process. In other cases, due to the closeness of ionic radii, the replacement of Fe(II) and Al(III) with Pb(II) is possible during adsorption. Furthermore, after adsorption and the passage of current during the electrochemical analysis, the Pb(II) ions are reduced to their corresponding atoms, which are then stripped from the electrode surface and released again into the electrolytic medium.

4. Conclusion

The paper reported for the first time the use of cyclic voltammetry (CV) and Linear Scan Anodic Stripping Voltammetry (LSASV) for the study of the mechanism of filtration of Pb(II) at the surface of a microfiltration ceramic membrane made from a lamp of a clay mineral. Bare graphite and clay-modified CPE sintered at temperatures ranging between 250 °C and 1100 °C were used as models to imitate what happens at the surface of the microfiltration ceramic membranes. Different weight percent of the clay membrane were crashed and mixed with pure graphite to obtain different CPE electrodes. 5 % clay is presented with the highest current peak, hence was selected as the optimal clay load for all subsequent studies as compared to other loads (1, 3, and 10 wt%). Pb(II) ion was found to accumulate well at the clay membrane/electrode surface at low pH of 1.5, however because of low chemical strength of the membrane, acetate buffer with pH = 4.5 was adopted as an optimal pH to study the filtration mechanism of Pb(II). At higher pHs (pH > 7), Pb(II) is found to precipitate as $Pb(OH)_2$ leading to no accumulation of Pb(II) at the surface of the clay membrane/electrode. Moreover, the membrane/electrode and the lead hydroxides ($Pb(OH)_3^-$) both develop an overall negative charge at high pH values, triggering electrostatic repulsions between the clay surface and the $Pb(OH)_3^-$ ions. It was also demonstrated that the clay is responsible for enhancing the electrochemical surface area of the electrode by 3-folds when GR is doped with the natural clay. The sintered clay @1000 °C, which represent the membrane surface, is found to be more selective to Pb(II) compared to Fe(II), the selectivity was attributed to grains fusion in the clay at high temperature and exchange of Pb(II) with Fe(II) and Al(III) existing in the clay structure. Given that, the mechanism of filtration of Pb(II) is dominated by charge repulsion, adsorption, and/or exchange capacity of the membrane. Careful attention must be paid to size exclusion dominated by the hydrated Pb(II) ion size. This study has proposed to study the mechanism of filtration of a single metal cation Pb(II), further studies are required on the filtration of this membrane in the presence of competitive cations.

Funding

This work is funded by the thesis support fund - College of Graduate Studies - University of Sharjah, United Arab Emirates, Graduate students support Grant No: student ID: 20105005, dated 16/12/2021.

CRediT authorship contribution statement

Lubna Jaber: Investigation, Data curation, Validation, Formal analysis, Investigation, Writing – original draft, Writing – review & editing. **Abdelaziz Elgamouz:** Conceptualization, Methodology, Validation, Formal analysis, Resources, Data curation, Writing – original draft, Writing – review & editing, Visualization, Supervision, Project administration, Funding acquisition. **Abdel-Nasser Kawde:** Conceptualization, Methodology, Validation, Formal analysis, Investigation, Resources, Data curation, Writing – original draft, Writing – review & editing, Visualization, Supervision, Project administration, Funding acquisition.

Declaration of Competing Interest

The authors declare that they have no known competing financial interests or personal relationships that could have appeared to influence the work reported in this paper.

Acknowledgments

The authors acknowledge the Graduate Students Support Grant No, Student ID: 20105005, dated 16/12/2021 and the Center for Advanced Materials Research Center at the University of Sharjah for TGA, X-ray diffraction, XRF, FT-IR, and SEM/EDS analysis.

Appendix A. Supplementary material

Supplementary data to this article can be found online at https://doi.org/10.1016/j.arabjc.2022.104303.

References

Aboudi Mana, S.C., Hanafiah, M.M., Chowdhury, A.J.K., 2017. Environmental characteristics of clay and clay-based minerals. Geol. Ecol. Landscapes 1 (3), 155–161. https://doi.org/10.1080/24749508.2017.1361128.

Afkhami, A., Soltani-Felehgari, F., Madrakian, T., Ghaedi, H., Rezaeivala, M., 2013. Fabrication and application of a new modified electrochemical sensor using nano-silica and a newly synthesized Schiff base for simultaneous determination of Cd2+, Cu2+ and Hg2+ ions in water and some foodstuff samples. Anal. Chim. Acta 771, 21–30. https://doi.org/10.1016/j.aca.2013.02.031.

Akanji, S.P., Arotiba, O.A., Nkosi, D., 2019. Voltammetric determination of Pb(II) ions at a modified Kaolinite-carbon paste electrode. Electrocatalysis 10 (6), 643–652. https://doi.org/10.1007/s12678-019-00552-3.

Altunay, N., Elik, A., Gürkan, R., 2019. Monitoring of some trace metals in honeys by flame atomic absorption spectrometry after ultrasound assisted-dispersive liquid liquid microextraction using natural deep eutectic solvent. Microchem. J. 147, 49–59. https://doi.org/10.1016/j.microc.2019.03.003.

Alves Xavier, L., de Oliveira, T.V., Klitzke, W., Mariano, A.B., Eiras, D., Vieira, R.B., 2019. Influence of thermally modified clays and inexpensive pore-generating and strength improving agents on the properties of porous ceramic membrane. Appl. Clay Sci. 168, 260–268. https://doi.org/10.1016/j.clay.2018.11.025.

Aoki, K.J., Chen, J., Liu, Y., Jia, B., 2020. Peak potential shift of fast cyclic voltammograms owing to capacitance of redox reactions. J. Electroanal. Chem. 856. https://doi.org/10.1016/j.jelechem.2019.113609.

Aragay, G., Merkoçi, A., 2012. Nanomaterials application in electrochemical detection of heavy metals. Electrochim. Acta 84, 49–61. https://doi.org/10.1016/j.electacta.2012.04.044.

V. Balek and M. Murat, "The emanation thermal analysis of kaolinite clay minerals," *Thermochim. Acta*, vol. 282–283, no. SPEC. ISS., pp. 385–397, 1996, doi: 10.1016/0040-6031(96)02886-9

Blaise, N. et al, 2022. Simultaneous electrochemical detection of Pb and Cd by carbon paste electrodes modified by activated clay. J. Anal. Methods Chem. 2022. https://doi.org/10.1155/2022/6900839.

Bodkhe, G.A. et al, 2021. Selective and sensitive detection of lead Pb (II) ions: Au/SWNT nanocomposite-embedded MOF-199. J. Mater. Sci. 56 (1), 474–487. https://doi.org/10.1007/s10853-020-05285-z.

Byers, H.L., McHenry, L.J., Grundl, T.J., 2019. XRF techniques to quantify heavy metals in vegetables at low detection limits. Food Chem. X 1. https://doi.org/10.1016/j.fochx.2018.100001.

Chen, Y.F., Wang, M.C., Hon, M.H., 2004. Phase transformation and growth of mullite in kaolin ceramics. J. Eur. Ceram. Soc. 24 (8), 2389–2397. https://doi.org/10.1016/S0955-2219(03)00631-9.

Choi, S.H. et al, 2019. Heavy metal determination by inductively coupled plasma-mass spectrometry (ICP-MS) and direct mercury analysis (DMA) and arsenic mapping by femtosecond (fs)–laser ablation (LA) ICP-MS in cereals. Anal. Lett. 52 (3), 496–510. https://doi.org/10.1080/00032719.2018.1471484.

Chooto, P., 2019. Cyclic voltammetry and its applications. Voltammetry.

Cui, L., Wu, J., Ju, H., 2015. Electrochemical sensing of heavy metal ions with inorganic, organic and bio-materials. Biosensors Bioelectron. 63, 276–286. https://doi.org/10.1016/j.bios.2014.07.052.

A. Elgamouz, N. Tijani, I. Shehadi, K. Hasan, and M. Al-Farooq Kawam, "Characterization of the firing behaviour of an illite-kaolinite clay mineral and its potential use as membrane support," *Heliyon*, vol. 5, no. 8, 2019, doi: 10.1016/j.heliyon.2019.e02281.

A. Elgamouz, N. Tijani, I. Shehadi, K. Hasan, and M. Al-Farooq Kawam, "Dataset of multiple methodology characterization of an illite-kaolinite clay mineral for the purpose of using it as ceramic membrane supports," *Data Br.*, vol. 29, 2020, doi: 10.1016/j.dib.2020.105300.

Elgamouz, A., Tijani, N., 2018. From a naturally occurring-clay mineral to the production of porous ceramic membranes. Microporous Mesopor. Mater. 271, 52–58. https://doi.org/10.1016/j.micromeso.2018.05.030.

Elgamouz, A., Tijani, N., 2018. Dataset in the production of composite clay-zeolite membranes made from naturally occurring clay minerals. Data Br. 19, 2267–2278. https://doi.org/10.1016/j.dib.2018.06.117.

El-Kordy, A. et al, 2022. Preparation of sodalite and faujasite clay composite membranes and their utilization in the decontamination of dye effluents. Membranes (Basel) 12 (1), 12. https://doi.org/10.3390/membranes12010012.

Fan, P., Zhen, K., Zan, Z., Chao, Z., Jian, Z., Yun, J., 2016. Preparation and development of porous ceramic membrane supports fabricated by extrusion technique. Chem. Eng. Trans. 55, 277–282. https://doi.org/10.3303/CET1655047.

Feldmann, J., Salaün, P., Lombi, E., 2009. Critical review perspective: elemental speciation analysis methods in environmental chemistry-moving towards methodological integration. Environ. Chem. 6 (4), 275–289. https://doi.org/10.1071/EN09018.

Gumpu, M.B., Sethuraman, S., Krishnan, U.M., Rayappan, J.B.B., 2015. A review on detection of heavy metal ions in water - an electrochemical approach. Sensors Actuators, B: Chem. 213, 515–533. https://doi.org/10.1016/j.snb.2015.02.122.

Guo, Z. et al, 2016. Functionalized porous Si nanowires for selective and simultaneous electrochemical detection of Cd(II) and Pb(II) ions. Electrochim. Acta 211, 998–1005. https://doi.org/10.1016/j.electacta.2016.06.141.

Hashemi, S.A. et al, 2022. Simultaneous electrochemical detection of Cd and Pb in aquatic samples via coupled graphene with

brominated white polyaniline flakes. Eur. Polym. J. 162. https://doi.org/10.1016/j.eurpolymj.2021.110926.
Hérold, C., Lagrange, P., 2003. Composés d'intercalation du graphite: Des binaires aux ternaires. Comptes Rendus Chim. 6 (4), 457–465. https://doi.org/10.1016/S1631-0748(03)00070-5.
Huo, D. et al, 2022. Three-dimensional graphene/amino-functionalized metal–organic framework for simultaneous electrochemical detection of Cd(II), Pb(II), Cu(II), and Hg(II). Anal. Bioanal. Chem. 414 (4), 1575–1586. https://doi.org/10.1007/s00216-021-03779-6.
Inglezakis, V.J., Loizidou, M.D., Grigoropoulou, H.P., 2003. Ion exchange of Pb2+, Cu2+, Fe3+, and Cr3+ on natural clinoptilolite: selectivity determination and influence of acidity on metal uptake. J. Colloid Interface Sci. 261 (1), 49–54. https://doi.org/10.1016/S0021-9797(02)00244-8.
Ito, A., Wagai, R., 2017. "Global distribution of clay-size minerals on land surface for biogeochemical and climatological studies". Sci. Data 4 (1). https://doi.org/10.1038/sdata.2017.103.
Kapoor, D., Singh, M.P., 2020. "Heavy metal contamination in water and its possible sources". Heavy Metals Environ.: Impact Assess., Remediat., 179–189
Khemakhem, I., Gargouri, O.D., Dhouib, A., Ayadi, M.A., Bouaziz, M., 2017. Oleuropein rich extract from olive leaves by combining microfiltration, ultrafiltration and nanofiltration. Sep. Purif. Technol. 172, 310–317. https://doi.org/10.1016/j.seppur.2016.08.003.
Kumari, N., Mohan, C., 2021. Basics of clay minerals and their characteristic properties. Clay Clay Miner.
Kypritidou, Z., Argyraki, A., Chryssikos, G., Stamatakis, M., 2017. Interaction of clay materials with lead in aqueous solutions. Bull. Geol. Soc. Greece 50 (4), 2221. https://doi.org/10.12681/bgsg.14278.
Lahnafi, A., Elgamouz, A., Tijani, N., Shehadi, I., 2020. Hydrothermal synthesis of zeolite A and Y membrane layers on clay flat disc support and their potential use in the decontamination of water polluted with toxic heavy metals. Desalin. Water Treat. 182, 175–186. https://doi.org/10.5004/dwt.2020.25173.
Lahnafi, A., Elgamouz, A., Tijani, N., Jaber, L., Kawde, A.N., 2022. Hydrothermal synthesis and electrochemical characterization of novel zeolite membranes supported on flat porous clay-based microfiltration system and its application of heavy metals removal of synthetic wastewaters. Micropor. Mesopor. Mater. 334,. https://doi.org/10.1016/j.micromeso.2022.111778 111778.
Lima, T.M., Soares, P.I., do Nascimento, L.A., Franco, D.L., Pereira, A.C., Ferreira, L.F., 2021. "A novel electrochemical sensor for simultaneous determination of cadmium and lead using graphite electrodes modified with poly(p-coumaric acid)". Microchem. J. 168. https://doi.org/10.1016/j.microc.2021.106406.
Mohajeri, P., Smith, C., Selamat, M.R., Abdul Aziz, H., 2018. "Enhancing the adsorption of lead (II) by bentonite enriched with pH-adjusted Meranti sawdust". Water (Switzerland) 10 (12). https://doi.org/10.3390/w10121875.
Mohammed, M.Q., Ismail, H.K., Alesary, H.F., Barton, S., 2022. Use of a Schiff base-modified conducting polymer electrode for electrochemical assay of Cd(II) and Pb(II) ions by square wave voltammetry. Chem. Pap. 76 (2), 715–729. https://doi.org/10.1007/s11696-021-01882-7.
Moudam, O., El Gamouz, A., 2016. Delaying the degradation caused by water of dye-sensitized solar cells. Org. Electron. 36, 7–11. https://doi.org/10.1016/j.orgel.2016.05.026.
Mouiya, M. et al, 2017. Porous ceramic from Moroccan natural phosphate and raw clay for microfiltration applications. Desalin. Water Treat. 83, 277–280. https://doi.org/10.5004/dwt.2017.20832.
Mouiya, M. et al, 2019. Fabrication and characterization of a ceramic membrane from clay and banana peel powder: application to industrial wastewater treatment. Mater. Chem. Phys. 227, 291–301. https://doi.org/10.1016/j.matchemphys.2019.02.011.
Moutcine, A. et al, 2020. Preparation, characterization and simultaneous electrochemical detection toward Cd (II) and Hg(II) of a phosphate/zinc oxide modified carbon paste electrode. Inorg. Chem. Commun. 116. https://doi.org/10.1016/j.inoche.2020.107911.
Mukherjee, I., Singh, U.K., Singh, R.P., 2021. An Overview on Heavy Metal Contamination of Water System and Sustainable Approach for Remediation. In: In *Water Pollution and Management Practices*, pp. 255–277.
Na Kim, H., Xiu Ren, W., Seung Kim, J., Yoon, J., 2012. Fluorescent and colorimetric sensors for detection of lead, cadmium, and mercury ions. Chem. Soc. Rev. 41 (8), 3210–3244. https://doi.org/10.1039/c1cs15245a.
Nguetnkam, J.P., Kamga, R., Villiéras, F., Ekodeck, G.E., Razafitianamaharavo, A., Yvon, J., 2005. Assessment of the surface areas of silica and clay in acid-leached clay materials using concepts of adsorption on heterogeneous surfaces. J. Colloid Interface Sci. 289 (1), 104–115. https://doi.org/10.1016/j.jcis.2005.03.053.
Ns, A.K., Ashoka, S., Malingappa, P., 2018. Nano zinc ferrite modified electrode as a novel electrochemical sensing platform in simultaneous measurement of trace level lead and cadmium. J. Environ. Chem. Eng. 6 (6), 6939–6946. https://doi.org/10.1016/j.jece.2018.10.041.
Pengou, M., Ngassa, G.B.P., Boutianala, M., Tchakouté, H.K., Nanseu-Njiki, C.P., Ngameni, E., 2021. Geopolymer cement–modified carbon paste electrode: application to electroanalysis of traces of lead(II) ions in aqueous solution. J. Solid State Electrochem. 25 (4), 1183–1195. https://doi.org/10.1007/s10008-021-04897-y.
Pujol, L., Evrard, D., Groenen-Serrano, K., Freyssinier, M., Ruffien-Cizsak, A., Gros, P., 2014. "Electrochemical sensors and devices for heavy metals assay in water: the French groups' contribution". Front. Chem. 2. https://doi.org/10.3389/fchem.2014.00019.
Raghavendra, N. et al, 2021. Electrochemical sensor studies and optical analysis of developed clay based CoFe2O4 ferrite NPs. Sensors Int. 2. https://doi.org/10.1016/j.sintl.2021.100083.
RoyChoudhury, P., Majumdar, S., Sarkar, S., Kundu, B., Sahoo, G. C., 2019. Performance investigation of Pb(II) removal by synthesized hydroxyapatite based ceramic ultrafiltration membrane: bench scale study. Chem. Eng. J. 355, 510–519. https://doi.org/10.1016/j.cej.2018.07.155.
Saleh, T.A., Gupta, V.K., 2016. "An overview of membrane science and technology". Nanomater. Polym. Membr., 1–23
Samain, L. et al, 2014. Structural analysis of highly porous γ-Al2O3. J. Solid State Chem. 217, 1–8. https://doi.org/10.1016/j.jssc.2014.05.004.
Sato, H., Mikazu, Y., Hideki, Y., 1975. 'Kagaku-binran, Kisohen II' (Handbook of Chemistry, Basic Version II). J. Nucl. Sci. Technol. 33 (12), 1180–1195.
Selmi, A., Khiari, R., Snoussi, A., Bouzouita, N., 2021. Analysis of minerals and heavy metals using ICP-OES and FTIR techniques in two red seaweeds (Gymnogongrus griffithsiae and Asparagopsis taxiformis) from Tunisia. Biol. Trace Elem. Res. 199 (6), 2342–2350. https://doi.org/10.1007/s12011-020-02335-0.
Stawiski, B., 2014. Research regarding effectiveness of compaction by compressing dry mortar cement and ceramic. Procedia Eng. 91, 412–417. https://doi.org/10.1016/j.proeng.2014.12.085.
Suchet, J.P., 1960. Rayons atomiques, electronegativites et energies d'activation dans les composes semiconducteurs mineraux. J. Phys. Chem. Solids 16 (3–4), 265–278. https://doi.org/10.1016/0022-3697(60)90156-6.
Sun, Y.F., Jian-Wang, P.H., Li, M.Y., Huang, X.J., 2019. Highly sensitive electrochemical detection of Pb(II) based on excellent adsorption and surface Ni(II)/Ni(III) cycle of porous flower-like NiO/rGO nanocomposite. Sensors Actuators, B Chem. 292, 136–147. https://doi.org/10.1016/j.snb.2019.04.131.
Tag, K., Riedel, K., Bauer, H.J., Hanke, G., Baronian, K.H.R., Kunze, G., 2007. Amperometric detection of Cu2+ by yeast biosensors using flow injection analysis (FIA). Sensors Actuators, B Chem. 122 (2), 403–409. https://doi.org/10.1016/j.snb.2006.06.007.

Tchoffo, R., Ngassa, G.B.P., Doungmo, G., Kamdem, A.T., Tonlé, I. K., Ngameni, E., 2022. Surface functionalization of natural hydroxyapatite by polymerization of β-cyclodextrin: application as electrode material for the electrochemical detection of Pb(II). Environ. Sci. Pollut. Res. 29 (1), 222–235. https://doi.org/10.1007/s11356-021-15578-8.

Touzara, S., Amlil, A., Saâdane, H., Laghlimi, C., Chtaini, A., 2019. EDTA-modified carbon paste composite for electrochemical determination of Pb(II) ions. J. Mater. Sci. Eng. 8 (6), 1–5.

Touzara, S., El Mastour, J., Amlil, A., Chtaini, A., 2022. "Electrochemical detection of lead ions by 2-benzimidazolethiol-modified carbon paste electrode prepared by inset modification: a voltammetric study". Kem. u Ind. 3–4. https://doi.org/10.15255/kui.2021.046.

Turdean, G.L., 2011. Design and development of biosensors for the detection of heavy metal toxicity. Int. J. Electrochem. 2011, 1–15. https://doi.org/10.4061/2011/343125.

Veerabadran, N.G., Price, R.R., Lvov, Y.M., 2008. Tubule clay nanoreactor for template synthesis of silver nanoparticles tubule clay nanoreactor for template synthesis of silver nanoparticles. Polym. Mater. Sci. Eng. vol. 99, 566.

Wang, H.E. et al, 2012. Microwave-assisted hydrothermal synthesis of porous SnO2 nanotubes and their lithium ion storage properties. J. Solid State Chem. 190, 104–110. https://doi.org/10.1016/j.jssc.2012.02.016.

Wang, Y. et al, 2022. Stripping voltammetric determination of cadmium and lead ions based on a bismuth oxide surface-decorated nanoporous bismuth electrode. Electrochem. Commun. 136. https://doi.org/10.1016/j.elecom.2022.107233.

Wang, Y., Nie, Z., Li, X., Zhao, Y., Wang, H., 2021. Highly sensitive and selective electrochemical sensor based on porous graphitic carbon nitride/CoMn2O4 nanocomposite toward heavy metal ions. Sensors Actuators B Chem. 346. https://doi.org/10.1016/j.snb.2021.130539.

Zhou, W., Wu, P., Zhang, L., Yao, S., Zhu, D., Cai, Y., 2022. Layer-by-layer assembly of nanocomposite interlayers on a kaolin substrate for enhancing membrane performance of Pb(II) and Cd (II) removal. Sci. Total Environ. 820. https://doi.org/10.1016/j.scitotenv.2022.153149.

Zuo, X., Wang, D., Zhang, S., Liu, Q., Yang, H., 2018. "Intercalation and exfoliation of kaolinite with sodium dodecyl sulfate". Minerals 8 (3). https://doi.org/10.3390/min8030112.